A. Cohades, A. Cetin and A. Mortensen, "Designing laminated metal composites for tensile ductility", Materials and Design, Vol. 66, Part B, 5 February 2015, pp. 412-420; http://www.sciencedirect.com/science/article/pii/S0261306914006773 .

Designing laminated metal composites for tensile ductility

Amaël Cohades*, Arda Çetin, Andreas Mortensen

Laboratory of Mechanical Metallurgy, Institute of Materials, Ecole Polytechnique Fédérale de Lausanne, EPFL Station 12, CH-1015 Lausanne, Switzerland

Abstract

This contribution draws practical implications of a recently published estimation of the tensile ductility in laminated composites made of two ductile materials, typically metals or alloys, which harden as both the strain and the strain-rate increase. To this end, the literature is surveyed to collect values for the strain hardening exponent, the strain-rate sensitivity and the strength constant for a wide range of engineering metals and alloys. Material combinations that might produce ductile laminated metal composites are then examined in light of the data and theory. A simple graph is proposed, which gives a direct reading of the predicted elongation to failure of composites containing equal volume fractions of any two materials among those surveyed. The resulting plots show material combinations in which a more ductile material can significantly increase, within a Laminated Metal Composite (LMC), the tensile elongation of a less ductile material. In this role, 304 stainless steel and commercial purity iron emerge as sensible possibilities.

Keywords: Composite, Laminated metal composite, ductility, strain-hardening, strain-rate hardening, elongation

1. Introduction

Of the many variables that govern the tensile elongation of ductile materials, strain-rate hardening is that which exerts the most dramatic influence: even small increases in a ductile material's strain-rate parameter m can strongly increase its tensile elongation; very high m values, roughly above 0.3, will even make it superplastic. How strain-rate hardening increases the elongation of materials is not simple: it does so, not by delaying the onset of instability (as work hardening does), but by retarding the consequences of necking. This makes the effect visible in experimental data: a typical signature of elongation driven by strain-rate hardening is the presence, in tensile stress-strain curves, of a long stage of deformation after the applied load has peaked [1–4]. This feature of the influence exerted by strain-rate hardening on tensile ductility complicates its analysis because one must examine the course of events beyond the onset of instability, at which a neck starts elongating faster than the remainder of a tensile bar. Linear stability analysis is then essentially useless, a fact that was identified and explained by Hutchinson and co-workers [1,4], who simultaneously with Ghosh [3] proposed a non-linear analysis of the deformation of strain-rate sensitive tensile bars under what is known as the long-

*Corresponding author
Telephone: +41 21 693 5995
E-mail: amael.cohades@epfl.ch

wavelength approximation. This separates the bar in two collinear regions, one slightly thinner than the other, and then integrates their collective deformation behaviour assuming uniform tensile stress across any section normal to the applied load. These assumptions make the problem tractable using simple numerical methods, and show how strain-rate sensitivity delays the transition to unstable thinning of the thinner portion in this two-zone description of a necked tensile bar.

In a recent paper, this analysis was extended to tackle, in general terms, the uniaxial tensile deformation of equistrain composites (*e.g.,* laminated composites stressed along their plane of lamination, or fibre composites stressed along their axis) made of two strongly bonded work hardening and strain-rate sensitive ductile materials (generally, but not necessarily, of metal) [5]. To distinguish these from the composite material, each of these two bonded materials making the composite is called a "phase" in what follows, even though these might, by themselves, be multiphased. Here, practical implications of the analysis are examined, to probe how it can aid the design of ductile Laminated Metal Composites (LMCs), originally reviewed by Sherby, Wadsworth et al. [6,7], more recent reviews being in Refs. [8, 9, 10]. This is done by gleaning literature data for the governing parameters *K, n* and *m* of a variety of metals and alloys, and then using these as input to identify combinations that might (or might not) hold promise for the design of ductile metallic LMCs. The article begins with a brief overview of the model, and then turns to its use and its implications.

2. Governing Equations

Consider a composite made of two components: A (a ductile phase) and B (a less ductile phase), Fig. 1. The two are strongly bonded and resist delamination as the composite deforms. Parallel to the plane of lamination, the flow stress of layered composites can reasonably be assumed to obey the rule-of-mixtures:

$$\sigma_{LMC} = V_A\sigma_A + V_B\sigma_B \qquad (1)$$

where σ_A and σ_B are respectively the stress in each of the two phases A or B when it is deformed to the average tensile strain of the composite, ε; the same rule of course applies also to aligned fibre composites pulled along the fibres. Parameters V_A and V_B=1-V_A are the volume fractions of Phases A and B respectively, and σ_{LMC} is the true (average) stress acting on the multilayered composite along the direction of applied stress. The two phases, A and B, are assumed to be distributed on a scale sufficiently fine that their stress and strain state always remain uniform across each cross-section of the composite normal to the stress axis, yet sufficiently large that their mechanical behaviour remain unaffected by plasticity size effects (so that data from bulk materials testing, reviewed below, can be used).

Following Hutchinson and Neale [1], the tensile specimen is assumed to have a uniform cross sectional area, exception made for a reduced (also called "non-uniform") section of cross-sectional area only a small fraction η smaller than the remaining, main "uniform" part of the same section. The long-wavelength assumption takes it that the transition to this reduced section is sufficiently gradual for the stress to be everywhere uniaxial. The gage section of the tensile bar is thus made of two colinear regions, one slightly wider and much longer than the other, the latter being of thinner cross section and destined to become the necking region of the tensile bar. Axial load equilibrium between the uniform and non-uniform portions dictates:

$$[V_A\sigma_A + V_B\sigma_B]A = \left[V_A\sigma_{A,0} + V_B\sigma_{B,0}\right]A_0 \tag{2}$$

where A and A_0 are the instantaneous cross-sectional areas of the reduced and uniform sections respectively, and all quantities associated with the uniform portion are denoted, in Eq. (2) and in all that follows, with a subscript 0. By definition, the initial fractional non-uniformity is:

$$\eta = \frac{A_{0,in} - A_{in}}{A_{0,in}} \tag{3}$$

with A_{in} and $A_{0,\text{in}}$ the initial cross sectional area of the reduced and uniform portions of the gauge section, respectively. Assuming constant volume, the true strain in the reduced (ε) and uniform (ε_0) portions of the considered sections is related to their cross-sectional areas (A, A_0) or lengths (L, L_0) by:

$$\varepsilon = -ln\frac{A}{A_{in}} = ln\frac{L}{L_{in}}, \qquad \varepsilon_0 = -ln\frac{A_0}{A_{0,in}} = ln\frac{L_0}{L_{0,in}} \tag{4}$$

Combining Eqs. (3) and (4) with Eq. (2) leads to:

$$V_A\sigma_A + V_B\sigma_B = \frac{e^{\varepsilon-\varepsilon_0}}{1-\eta}\left[V_A\sigma_{A,0} + V_B\sigma_{B,0}\right] \tag{5}$$

To describe the time-dependent flow stress of the two phases making the laminate, a customary constitutional law is adopted, in which contributions from strain hardening and strain-rate hardening to the flow stress are added [1][3]:

$$\sigma = K\left[\varepsilon^n + m\ ln\left(\frac{\dot{\varepsilon}}{\dot{\varepsilon}_R}\right)\right] \tag{6}$$

Here K is the strength constant, n the strain-hardening exponent, m the strain-rate hardening constant and $\dot{\varepsilon}_R$ a reference strain-rate, typically given by the value $5\text{x}10^{-5}$ s^{-1} [3]. This description of the material's flow stress is convenient in the context of composites, as will be seen below. It also has a physical grounding, in that the strain-rate sensitivity m in Eq. (6) is directly related to the (measurable) activation volume V_{a} characteristic of the thermally activated event that governs the strain-rate dependence of plastic flow:

$$mK = \frac{MkT}{V_a} \tag{7}$$

where kT has the usual meaning. Writing Eq. (6) for the two phases A and B and inserting these two equations into Eq. (5) gives:

$$e^{-\varepsilon}\left[V_A K_A \varepsilon^{n_A} + V_B K_B \varepsilon^{n_B} + (V_A K_A m_A + V_B K_B m_B) ln\left(\frac{\dot{\varepsilon}}{\dot{\varepsilon}_R}\right)\right] = \frac{e^{-\varepsilon_0}}{1-\eta}\left[V_A K_A \varepsilon_0^{n_A} + V_B K_A \varepsilon_0^{n_B} + (V_A K_A m_A + V_B K_B m_B) ln\left(\frac{\dot{\varepsilon}_0}{\dot{\varepsilon}_R}\right)\right] \quad (8)$$

for the composite in the long-wave length assumption. Two dimensionless parameters then emerge:

$$\beta = \frac{V_A K_A}{V_A K_A + V_B K_B} \quad (9)$$

$$\mu = \beta m_A + (1-\beta) m_B \quad (10)$$

which, when inserted into Eq. (8), turn it into:

$$ln\left(\frac{\dot{\varepsilon}}{\dot{\varepsilon}_R}\right) = \frac{e^{\varepsilon-\varepsilon_0}}{1-\eta}\left[\frac{\beta\varepsilon_0^{n_A} + (1-\beta)\varepsilon_0^{n_B}}{\mu} + ln\left(\frac{\dot{\varepsilon}_0}{\dot{\varepsilon}_R}\right)\right] - \frac{\beta\varepsilon^{n_A} + (1-\beta)\varepsilon^{n_B}}{\mu} \quad (11)$$

This gives, for a given level of deformation (at which the uniform and reduced sections have respectively reached strains ε_0 and ε), the relation between instantaneous strain increments in the two regions of the tensile bar. Assuming then a fixed strain-rate in the uniform section of the tensile sample gage length (*i.e.*, that $\dot{\varepsilon}_0$ is constant), the deformation in the reduced section can be deduced by numerical integration across small time steps. At some point $\dot{\varepsilon}$ diverges rapidly to infinity: this is when the tensile bar breaks.

This succession of events is depicted in Fig. 1, which depicts a homogeneous composite of two finely divided continuous phases that are aligned along the axis of the tensile bar, such that the equistrain rule of mixtures applies everywhere. One region of the tensile bar is slightly narrower than the rest. The inhomogeneity being small, as the bar is pulled the two regions deform at first together, with strain in the imperfection only slightly higher than in the remainder of the bar. Past a certain point, the strain in the narrower section increases without limit, while deformation stops in the remainder of the bar: necking has then begun and the homogeneous region of the bar has reached its failure strain.

Assuming constant volume, if L and L_o are, respectively, the length of the reduced and uniform sections of the tensile bar gage section, the measured (engineering) strain of the tensile bar at failure is:

$$elongation = \frac{L_o(e^{\varepsilon_o} - 1) + L(e^{\varepsilon} - 1)}{L_o + L} \tag{12}$$

If $L << L_o$, since in practice the reduced section will fail at some finite value of ε, this roughly equals the elongation in the uniform section of the bar, $(e^{\varepsilon_o} - 1)$. Otherwise, if choices or assumptions are made regarding (i) the ratio between L and L_o and (ii) the (finite) value of ε at which the reduced section breaks, then the measured elongation of a given tensile bar can be calculated (*e.g.,* Ref. [11]). Here, the uniform section elongation ε_0 at the transition towards very large ε is adopted as a measure of the material's ductility, because this quantity is free of assumptions concerning L, L_0, or the precise value of ε at which the neck fails. Resulting ε_0–based elongation values are a lower bound for the total ductility that will be measured in any given tensile bar, for two reasons: (i) ε exceeds ε_0, and (ii) the fact that near the point at which the applied tensile load peaks, the slope of the true stress true strain curve is also low. This causes the small difference in stress between the uniform and reduced sections (coming from their initial difference in area) to translate into a significant difference in corresponding strain values. In particular, since when $m = 0$ the transition occurs when $\varepsilon = n$ [1], corresponding values of ε_0 will therefore be smaller than n, to an extent that depends on the chosen (small) value of η that was assumed in the calculations.

Returning to Eq. (11), one notices that it combines four independent parameters (V_A, K_A/K_B, m_A, m_B) into two parameters only: β and μ. The latter parameter is a single descriptor of the strain-rate sensitivity of the composite, which emerges directly from the governing equations (this is why the law in Eq. (6) is more convenient here than the more usually adopted power-law dependence of stress on strain-rate). The former parameter, β, is essentially a measure of the relative load-bearing capacity of Phase A within the composite [5].

It was shown in Ref. [5], by calculating numerically the elongation of the binary composite for a variety of combinations of the four remaining governing parameters (β, μ, n_A, n_B), that the composite essentially elongates as does a uniform material deforming according to Eq. (6) if its value of m is given as μ in Eq. (10) and its strain hardening exponent n equals ν defined as:

$$\upsilon = \beta n_A + (1 - \beta) n_B \tag{13}$$

i.e., by the same "load-bearing fraction" modulated rule of mixtures as that which defines μ.

This β-modulated identical "load-bearing fraction modulated rule of mixture" estimate of an effective n and m describing the elongation of the composite (which is rigorously obeyed if linear hardening is assumed or if both phases have the same value of n [5]) implies that, on a graph having n and m as coordinates, a composite of two materials situated at points A and B will behave as a third material situated at point C along the straight line joining point A to point B such that:

$$\beta = \frac{BC}{AB} \tag{14}$$

Using a Taylor-series-based explicit finite difference algorithm with fixed strain increments $\Delta\varepsilon_0 = 0.0001$, and calculating the value of ε at each strain increment using the bisection method with an error of 10^{-10} for $\dot{\varepsilon}_0$ set to 10^{-4} s^{-1}, a graph was constructed that maps the predicted uniform strain to failure in coordinates of *m* versus *n*. This is given in Fig. 2, where the higher error region (in which using Eqs. (13) and (14) becomes inaccurate [5]) is indicated. This graph is now used, together with the equations above, to examine a few practical cases based on a survey of literature data for *K*, *n* and *m*.

3. Materials Properties

3.1 – Literature data

Room-temperature uniaxial tensile deformation parameters are given from a survey of the literature in Table 1 for aluminium and copper alloys, Table 2 for iron-based alloys, and Table 3 for alloys based on magnesium, nickel, cobalt, tantalum or titanium. Data include values for the strain hardening exponent *n*, the strain-rate sensitivity *m*, the strength constant *K*, the process used to produce the metal or alloy, and its average grain size (*d*). Where available, values of the measured uniform tensile failure strain (ε_u EXP, excluding the neck) and/or the average tensile failure strain ($\varepsilon_{failure}$ EXP, including deformation in the neck) are also given. To extract these values from articles in the literature, the following methods and assumptions were used.

Where *K* and *n* were explicitely given by the authors, reported values are inserted directly into the tables. In such cases, *i.e.*, where authors report the method used to extract these values from their stress-strain data, all used a linear fit of the stress-strain curve in log-log coordinates. Most articles do not give *K* and *n* directly, however; more often, one finds plots of measured stress-strain curves. Values for *n* and *K* were then determined by the present authors, after digitization of published stress-strain curves using the *Datathief* software (http://datathief.org/). The work hardening exponent *n* was computed from the slope of a linear fit of log(σ)-log(ε) plots from reported stress-strain curves, the strength constant *K* being the value of σ where this fit intercepts the log(σ) axis. As this was the approach used in articles that give *K* and *n* directly wherever specifics were given for how these parameters were computed, this makes the dataset relatively consistent. Note that values of *K* and *n* in the tables are of necessity approximate and incomplete descriptors of the tensile flow law of the material, if only because the Hollomon equation is a pragmatic descriptor of stress-strain curves that is devoid of a physical foundation. In some instances *n* is far from constant along the stress-strain curve [2]; the calculated strain to failure will then vary significantly depending on how the fit is made. Where *n* was found to vary, therefore, the following convention was used in curve-fitting log(σ)-log(ε) plots: the linear fit to the curve was performed over a strain interval of 2% situated in the middle of the strain range extending from the material's recorded yield stress and its recorded Ultimate Tensile Strength (UTS).

Differences in the strain-rate parameter *m* that exist between the two usual deformation laws, namely $\sigma = K\varepsilon^n\dot{\varepsilon}^m$, in which case *m* is computed from measurements of the flow stress at two different strain-rates using:

$$m = \frac{\sigma_2 - \sigma_1}{\sigma \cdot \ln\left(\frac{\dot{\varepsilon}_2}{\dot{\varepsilon}_1}\right)} \tag{15}$$

and the law used here (Eq. (6)): $\sigma = K\left[\varepsilon^n + m\ \ln\left(\frac{\dot{\varepsilon}}{\dot{\varepsilon}_r}\right)\right]$ where m is instead computed as:

$$m = \frac{\sigma_2 - \sigma_1}{K \cdot \ln\left(\frac{\dot{\varepsilon}_2}{\dot{\varepsilon}_1}\right)} \tag{16}$$

have been neglected. As seen by comparing Eqs. (15) and (16), the difference is in the ratio between the instantaneous flow stress at the time of measurement and the strength constant K. This difference can be compensated using an approximation (such as multiplying values derived using Eq. (15) by a factor $\frac{\sigma_{UTS}}{K}$); however, this was not deemed worthwhile given (i) uncertainty in values of σ_{UTS} or K, coupled with (ii) the fact that the difference between $\sigma_{\text{UTS}} \approx n^n \cdot K$ and K is relatively small since $n < 1$. Where m is reported in the literature, it was always computed using Eq. (15). Where m was determined experimentally by the present authors (this is indicated with [-] in lieu of a reference number in Tables 1 to 3), it was computed using Eq. (16) after deducing K and n as indicated above. Finally, it is emphasized that data were collected here without concern for the range of deformation rates covered in reported experiments: Tables 1 to 3 thus include data from dynamic tests conducted at very high strain rates.

Reports of the elongation to failure vary with the reference. At times it is not clear whether values reported for the tensile elongation correspond to the uniform strain to failure or to the average strain at failure for the tensile bars tested (including then deformation in the neck). In case of doubt, the reported failure strain was placed in the column for the uniform strain to failure (ε_u EXP) in the tables (where it will represent an upper bound for ε_u EXP).

3.2 – Materials and their characteristics

An additional column in the tables gives the theoretical uniform strain (ε_u TH) predicted by the long wavelength analysis with η = 0.005 using reported values of K, n and m for each material. Calculations of ε_u TH were of course all performed using tabulated values of n and m in the flow law given by Eq. (6), assuming $\frac{\dot{\varepsilon}_0}{\dot{\varepsilon}_R} = 2$ and η=0.005.

Examination of the tables shows that measured uniform strains (ε_u EXP) are all smaller than values calculated by the model (ε_u TH), often significantly so. This is a combined result of uncertainty in parameter values, of limitations inherent to the long-wavelength analysis (neck regions are typically not much longer than they are wide, making the assumed uniaxial stress state a crude approximation in later stages of necking) and of the influence exerted by many other potential factors (premature failure in the neck due to damage percolation, greater shape inhomogeneity along the gage section than was assumed with the chosen value of η, *etc.*). What follows is, therefore, to be taken as an indicator of pathways for composite design rather than precise predictions of the elongation to failure of a given material or LMC.

With these caveats enounced, materials of Tables 1 to 3 are placed on the map of predicted uniform strains to failure given in Fig. 2. This is obviously done by placing each point at its relevant set of n and m coordinates; however, each point is additionally given an area that is proportional to the corresponding value of K. This makes visible the load-bearing capacity of each phase, and hence its weight when β is computed. This device also allows the reader to eyeball on the plot where an LMC

made of equal volume fractions of two alloys A and B is located: it is to be placed along the straight line joining points corresponding to A and B at the point where a fulcrum will balance the two circles surrounding points for A and B, treated as masses at the end of the line assimilated to a rigid rod, as sketched in Fig. 3. Of course, for other phase volume fractions, Eq. (16) remains valid and the point for the LMC can be placed on the graph by calculating β knowing V_A and values for K in Tables 1 to 3 using Eqs. (9), (10) and (13). The result is in Fig. 4, where different colours have been additionally used to distinguish different alloy families by their primary ingredient.

Aluminium alloys (the red circles in Fig. 4) have moderate formability and strength compared, for example, to steel [3,12]. Their flow stress is known to be generally insensitive to the strain-rate [2]; corresponding data points lie therefore at the bottom of Fig. 4. Their flow stress is also well below that of steels: data points are therefore surrounded by correspondingly small circles.

Copper and its alloys (magenta in Fig. 4) have variegated strain hardening properties: a low to moderate strain hardening exponent coupled with significant strain-rate sensitivity, or conversely, high n but low m. The former case corresponds to nanocrystalline copper, produced by various relatively complex manufacturing processes. The latter case is characteristic of coarser grained copper and of industrial copper alloys produced by more conventional manufacturing processes such as rolling. One data point is situated in the middle of these two families: this is for copper containing a high density of nano-twinned lamellae produced by pulsed electrodeposition, which combines a high strain-hardening capacity with a high sensitivity to strain-rate, giving the material an attractive combination of strength and ductility [13].

Pure iron (yellow in Fig. 4) is a soft material, but it is ductile. It is characterized by a limited strain-hardening capacity ($n \leq 0.3$) and low strength constants when processed by conventional manufacturing techniques. Its strength can be increased by reducing the grain size; however this does not always increase its ductility and necessitates, at the finest grain size values, relatively complex manufacturing techniques [14,15].

Steel, in its many variants (green in Fig. 4) is overall characterized by a low sensitivity to strain-rate ($m \leq 0.02$ even at low grain sizes), a finite work hardening capacity ($n < 0.3$) with comparatively high values of K. The strain hardening capacity of type 300 austenitic stainless steels depends on whether martensite forms during deformation [16]. Austenitic 304 stainless steel has a high strain hardening capacity, which places it to the far right of the graph, and a high strength constant K, which gives it a big circle on the graph – and hence a dominant role within LMCs.

Magnesium alloys (grey in Fig. 4) have moderate ductility and a low strength constant; interest in using these alloys in LMCs comes from the low density of magnesium [17]. Nickel, cobalt and tantalum have relatively similar properties: a limited work hardening capacity ($n \leq 0.3$) coupled with a significant strength constant (mainly due to the small grain size that can be achieved using complex manufacturing processes). The flow stress sensitivity to strain-rate is limited for nickel and cobalt. For tantalum m is higher; however, n is low, which gives the metal a low ductility. Decreasing the grain size of tantalum has a negative influence on the strain-rate sensitivity, unlike copper for example [18].

Finally, titanium alloys have low ductility, low sensitivity to strain-rate, limited strain-hardening capacity and intermediate strength constants. Note that using these alloys in the present model has to be more tentative as their properties fall within the high error region of the model (Figs. 2 and 4) [5].

These literature data are also collated in graphs giving n (Fig. 5) or m (Fig. 6) versus the grain size d, again using the convention whereby each point is represented with a circle, the area of which is proportional to K. As seen, although the strain-rate sensitivity increases in general as d decreases [19], as does the strength constant K for a given alloy system, trends are not simple or uniform: exceptions are found for iron, copper and aluminium alloys, many among these being alloys hardened by heat treatment.

4. Composite Design

4.1 – General considerations and methodology

Turning back to Fig. 4, let us examine what opportunities one may find for the design of ductile LMCs: what alloys or metals would one be tempted to pair in a laminated composite, with a goal of creating a new material that has (in theory at least) an attractive combination of strength and ductility ? In general terms, the exercise will be one of pairing a low-ductility material (Material B) with another material (Material A) that can "coax" it towards higher elongations. Looking at the graph and at the analysis in Section 2, a few general rules emerge:

(i) low-ductility metals and alloys (Material B) are predominantly ones with low n values: high m will make a ductile material (potentially much) more ductile, but will not *per se* give it a high elongation unless m is very high (as is the case with superplastic materials [2]);

(ii) to coax any such less ductile Material B towards higher elongations, Material A must have a sufficiently high strength constant K in comparison with that of Material B: otherwise, the composite will have values of ν and μ, and hence an elongation, that remain near values characteristic of Material B (Eqs. (9), (10) and (13)) no matter where Material A may be situated on the graph;

(iii) if Material B is situated near the lower-left corner of the ductility map (Figs. 2 and 4), Material A is optimally situated along the normal to iso-ductility lines stretching from the point representing Material B. In other words Material A is then optimally in the region of simultaneously high n and m; however, the choice of such materials is limited, and opportunities also exist with materials that have very high n and low m coupled with sufficiently high K, such as 304 stainless steel.

(iv) If Material B has a low ductility because it has a low strain-hardening exponent n while having a finite strain-rate hardening constant m (or in other words if it lies near the vertical axis of the graph), then Material A need only have a reasonably high value of n; in other words it may lie near the horizontal axis provided it is remote from the origin. The combination then might have a ductility that exceeds that of both of its constituents.

4.2 – Specific combinations

Looking at Fig. 4 one finds that many alloys among those surveyed here are clustered near the lower left corner of the graph: these are potential candidates as Material B. Interesting alloys for Material A are then ones for which points are situated away from this corner, in or beyond the green iso-elongation bands in the figure. These are metals and alloys with either a very high n, or a combination of reasonable n and finite m. On closer examination one finds that several points for steel, iron and copper are good candidates as a "coaxing or A" constituent that may, in a strongly bonded LMC, elongate a less ductile alloy. In the other role, meaning for the less ductile "coaxed or B" material, three materials are selected as examples. These phases as well as some of their potential LMC partner

materials are drawn in Figure 7, where points of mixed colour indicate 50-50 combinations of the two materials situated at the end of the dotted line passing through the mixed colour point.

6XXX aluminium alloys have moderate ductility (leading to more limited formability compared, for example, with steel) and, as visible on the graph, a limited strength constant *K*. Let us take them as Material B in an LMC. Nanotwinned copper lies roughly along the normal to equistrain lines from where these alloys are situated. This makes it a potent Material A partner for these alloys. From a practical standpoint the combination will suffer in many structural applications from the high density of copper. On the positive side, note that producing electrodeposited nanotwinned copper in a three-layer LMC using a thin sheet of the other metal for the initial cathode is a convenient way of processing the nanotwinned metal. Two other options are iron-based. One is ductile pure iron : the predicted strain to failure in an LMC containing equal volume fractions of 6XXX aluminium alloy and ductile iron is 0.35, over three times higher than for the monolithic aluminium alloy (Fig. 7). Another is austenitic 304 stainless steel: this will result in roughly the same composite failure strain although the steel has a monolithic strain to failure that is somewhat lower than for the iron considered previously. The reason for this is the higher *K* of 304 stainless steel. In practice, however, both combinations pose the significant challenge that between aluminium and all of iron, nickel or chromium, the driving force for the formation of brittle intermetallics is high (*e.g. Refs.* [20,21]). Although the mechanics are promising, their metallurgical engineering presents a challenge that is still being addressed.

Magnesium is a lightweight metal used in several applications; it has reasonable but still relatively low ductility. As seen on Fig. 7, similarly to 6XXX alloys, combining magnesium alloys with iron or 304 stainless steel can produce LMCs having a far higher ductility (and strength) than the magnesium alloy alone: in theory, if the two phases are perfectly bonded, the elongation can be increased to 0.2. Metallurgically, such LMCs pose less of a challenge at their interface with iron and its alloys than do aluminium alloys: Refs. [17,22,23] give examples of interfacial engineering in magnesium-steel LMCs produced by reactive transient liquid phase bonding, or by pressure infiltration, respectively. On the other hand the wet corrosion resistance of this LMC is dismal: to be usable it must be completely sealed from the environment with a protective coating.

Lastly, titanium is a material where a finite strain-rate sensitivity is not linked to a high ductility because of a low work-hardening capacity (translating into a low *n* value) [24]. Here, given the finite *m* value, nearly any combination with a phase having reasonable ductility will be of benefit: many metals and alloys in Fig. 4 will do. For example, bonding to copper or steel [25] will increase the predicted failure strain to 0.32 for the 50-50 combination with 304 stainless steel shown on the graph. Here again, however, the challenge lies in avoiding the formation of brittle intermetallics along the interface between the two metals [26,27]. Note also that many nanocrystalline alloys are similar to titanium, in that their finite strain-rate sensitivity is not coupled to a high work hardening capacity. These, too, therefore make good candidates as the less ductile Material B of an LMC in which the partner Material A need only have a high *n* value - coupled with high *K* given the high strength of most nanocrystalline metals and alloys.

More generally, the analysis and examples that precede emphasize the importance of a high load bearing capacity for any metal or alloy that is envisaged as the “ductile” partner in an LMC designed to elongate significantly before failing by necking. This also explains why combining a metal of low ductility with a polymer will only seldom produce a ductile material: *K* values are in general much lower for polymers than for metals. Exceptions are ones where the polymer is relatively strong and

sufficiently thick (an example being PMMA, with its flow stress around 200 MPa [28]) and/or where the metal deforms at low stress, either because it is cracked or because it is corrugate. Examples of such layered composites containing films of artificially compliant metal, designed to have a high elongation to failure for applications in flexible electronics, can be found in Refs. [11,29–31].

5. Conclusions

Three parameters are used to predict the tensile elongation of composites of strain and strain-rate sensitive materials that fail by necking and deform according to the equistrain rule of mixtures: these are the strength constant K, the strain hardening exponent n and the strain-rate sensitivity parameter m. Surveying the literature for values of these three constants and plotting these in (n, m) coordinates with points having an area proportional to K creates a map that can be used to read directly the predicted strain to failure of ductile-ductile LMCs combining any pair of two such materials in roughly equal proportions by volume. This map, in turn, shows how certain pairs are opportune while other pairs are less so; a key determinant in this is the ratio of K values for the two phases to be combined. Among materials surveyed, austenitic stainless steel and commercial purity iron result in attractive values of this ratio, making them attractive options as the ductility-enhancing component within a Laminated Metal Composite.

Acknowledgments

This work was sponsored by the Collaborative Research Programme between the University of Tokyo and the Ecole Polytechnique Fédérale de Lausanne supported by the Toyota Motor Corporation. The authors wish to thank Professors Toshihiko Koseki, Junya Inoue and Shoichi Nambu of the University of Tokyo, for many stimulating discussions and exchanges in the course of this collaboration. Finally we wish to point out that, although all data in this review were transcribed with care, we cannot guarantee that these are free of transcription errors; hence data listed herein should not be used for design (original source data should instead be used).

References

[1] Hutchinson JW, Neale KW. Necking under Uniaxial Tension. Acta Metallurgica 1977;25:839–46.

[2] Ghosh AK. The Influence of Strain Hardening and Strain-Rate Sensitivity on Sheet Metal Forming. Journal of Engineering Materials and Technology 1977;99:264–74.

[3] Ghosh AK. Tensile Instability and Necking in Materials with Strain Hardening and Strain-Rate Hardening. Acta Metallurgica 1977;25:1413–24.

[4] Hutchinson JW, Obrecht H. Tensile Instabilities in Strain-Rate Dependent Materials. Proceedings of the 4th International Conference on Fracture 1977;1:101–16.

[5] Çetin A, Bernardi C, Mortensen A. An analysis of the tensile elongation to failure of laminated metal composites in the presence of strain-rate hardening. Acta Materialia 2012;60:2265–76.

[6] Lesuer DR, Syn CK, Sherby OD, Wadsworth J, Lewandowski JJ, Hunt WH. Mechanical behaviour of laminated metal composites. International Materials Reviews 1996;41:169–97.

[7] Wadsworth J, Lesuer DR. Ancient and modern laminated composites - from the Great Pyramid of Gizeh to Y2K 2000;45:289–313.

[8] Koseki T, Inoue J, Nambu S. Development of multilayer steels for improved combinations of high strength and high ductility. Materials Transactions of the Japan Institute of Metals and Materials 2014; 55:227-237.

[9] Embury JD. Ferrous Composites. Annual Review of Materials Research 2010;40:213–41.

[10] Mortensen A, Llorca J. Metal Matrix Composites. Annual Review of Materials Research 2010;40:243–70.

[11] Pardoen T. Size and rate dependent necking in thin metallic films. Journal of the Mechanics and Physics of Solids 2014;62:81–98.

[12] Mahabunphachai S, Koç M. Investigations on forming of aluminum 5052 and 6061 sheet alloys at warm temperatures. Materials and Design 2010;31:2422–34.

[13] Lu L, Schwaiger R, Shan ZW, Dao M, Lu K, Suresh S. Nano-sized twins induce high rate sensitivity of flow stress in pure copper. Acta Materialia 2005;53:2169–79.

[14] Wei Q, Kecskes L, Jiao T, Hartwig KT, Ramesh KT, Ma E. Adiabatic shear banding in ultrafine-grained Fe processed by severe plastic deformation. Acta Materialia 2004;52:1859–69.

[15] Jia D, Ramesh KT, Ma E. Effects of nanocrystalline and ultrafine grain sizes on constitutive behavior and shear bands in iron. Acta Materialia 2003;51:3495–509.

[16] Krauss G. Martensite Formation, Strain Rate Sensitivity, and Deformation Behavior of Type 304 Stainless Steel Sheet. Metallurgical Transactions A 1989;20A:1239–46.

[17] Araki T, Koba M, Nambu S, Inoue J, Koseki T. Reactive Transient Liquid Phase Bonding between AZ31 Magnesium Alloy and Low Carbon Steel. Materials Transactions 2011;52:568–71.

[18] Wei Q, Cheng S, Ramesh KT, Ma E. Effect of nanocrystalline and ultrafine grain sizes on the strain rate sensitivity and activation volume : fcc versus bcc metals. Materials Science & Engineering A 2004;381:71–9.

[19] Cheng S, Ma E, Wang Y, Kecskes L, Youssef K, Koch C, et al. Tensile properties of in situ consolidated nanocrystalline Cu. Acta Materialia 2005;53:1521–33.

[20] Kyokuta N, Koba M, Araki T, Nambu S, Inoue J, Koseki T. Fracture Toughness Evaluation of Thin Fe-Al Intermetallic Compound Layer at Reactive Interface between Dissimilar Metals. Materials Transactions 2013;54:994–1000.

[21] Gladkvoskii S V, Trunina TA, Kokovikhin EA, Smirnova S V, Kamantsev IS, Gorbunov A V. Structural steel-aluminum sandwich composites based on low-carbon steel 006/IF. Metal Science and Heat Treatment 2013;55:3–7.

[22] Koba M, Araki T, Nambu S, Inoue J, Koseki T. Bonding Interface Formation between Mg Alloy and Steel by Liquid-phase Bonding using the Ag Interlayer. Metallurgical and Materials Transactions A 2012;43:592–7.

[23] Çetin A, Krebs J, Durussel A, Rossoll A, Inoue J, Koseki T, et al. Laminated Metal Composites by Infiltration. Metallurgical and Materials Transactions A 2011;42:3509–20.

[24] Neeraj T, Daehn GS, Mills MJ. Phenomenological and Microstructural Analysis of Room Temperature Creep in Titanium Alloys. Acta Materialia 2000;48:1225–38.

[25] Carreker RPJ, Hibbard WRJ. Tensile Deformation of High-Purity Copper as a Function of Temperature, Strain Rate, and Grain Size. Acta Metallurgica 1953;1:654–63.

[26] Moore JJ. Evaluation of Formable Light Metal-Alloy Steel Composites. Materials Science & Engineering 1981;48:123–36.

[27] Bokstein BS, Vnukov VI, Golosov E V. Structure and Diffusion Processes in Laminated Composites of a Cu-Ti System. Russian Physics Journal 2009;52:40–4.

[28] Bucaille JL, Gauthier C, Felder E, Schirrer R. The influence of strain hardening of polymers on the piling-up phenomenon in scratch tests: Experiments and numerical modelling. Wear 2006;260:803–14.

[29] Vandeparre H, Liu Q, Minev IR, Suo Z, Lacour SP. Localization of Folds and Cracks in Thin Metal Films Coated on Flexible Elastomer Foams. Advanced Materials 2013;25:3117–21.

[30] Vandeparre H, Watson D, Lacour SP. Extremely robust and conformable capacitive pressure sensors based on flexible polyurethane foams and stretchable metallization. Applied Physics Letters 2013;103:204103.

[31] Li T, Huang ZY, Xi ZC, Lacour SP, Wagner S, Suo Z. Delocalizing strain in a thin metal film on a polymer substrate. Mechanics of Materials 2005;37:261–73.

[32] Miyamoto H, Ota K, Mimaki T. Viscous nature of deformation of ultra-fine grain aluminum processed by equal-channel angular pressing. Scripta Materialia 2006;54:1721–5.

[33] Semiatin SL., Piehler HR. Deformation of Sandwich Sheet Materials in Uniaxial Tension. Metallurgical Transactions A 1978;10A:85–96.

[34] Kalpakjian S. Manufacturing Processes for Engineering Materials, Second Edition. Addison-Wesley; 1991.

[35] Khan AS, Huang S. Experimental and Theoretical Study of Mechanical Behaviour of 1100 Aluminum in the Strain Rate Range (10^-5) - (10^4) s-1. International Journal of Plasticity 1992;8:397–424.

[36] Takuda H, Fujimoto H, Hatta N. Formabilities of steel / aluminium alloy laminated composite sheets. Journal of Materials Science 1998;33:91–7.

[37] Kovács-Csetényi E, Horváth M, Chinh NQ, Kovács I. Effect of Grain Size on Tensile Stress and Ductility in Al99.99. Physica Status Solidi (a) 1998;166:805–10.

[38] Miles MP, Siles JL, Wagoner RH, Narasimhan K. A Better Sheet Formability Test. Metallurgical Transactions A 1993;24A:1143–51.

[39] Fields DS, Backofen WA. Temperature and Rate Dependence of Strain Hardening in the Aluminum Alloy 2024-O. Trans ASM 1959;51:946–60.

[40] Niranjani VL, Hari Kumar KC, Subramanya Sarma V. Development of high strength Al–Mg–Si AA6061 alloy through cold rolling and ageing. Materials Science and Engineering: A 2009;515:169–74.

[41] Sabirov I, Estrin Y, Barnett MR, Timokhina I, Hodgson PD. Enhanced tensile ductility of an ultra-fine-grained aluminum alloy. Scripta Materialia 2008;58:163–6.

[42] Gray III GT, Lowe TC, Cady CM, Valiev RZ, Aleksandrov I V. Influence of Strain-Rate & Temperature on the Mechanical Response of ultrafine Grained Cu, Ni and Al-4Cu-0.5Zr. Acta Metallurgica 1997;9:477–80.

[43] Lu L, Li SX, Lu K. An abnormal strain rate effect on tensile behavior in nanocrystalline copper. Scripta Materialia 2001;45:1163–9.

[44] Shen YF, Lu L, Dao M, Suresh S. Strain rate sensitivity of Cu with nanoscale twins. Scripta Materialia 2006;55:319–22.

[45] Dao M, Lu L, Shen YF, Suresh S. Strength, strain-rate sensitivity and ductility of copper with nanoscale twins. Acta Materialia 2006;54:5421–32.

[46] Champion Y, Langlois C, Guérin S, Duhamel C. Analysis of ductility of nanostructured copper prepared by powder metallurgy. Engineering Fracture Mechanics 2008;75:3624–32.

[47] Fernandes J, Menezes LF, Rodrigues DM, Chaparro BM, Vieira MF. Non-uniform deformation after prestrain. European Journal of Mechanics - A/Solids 2000;19:209–21.

[48] Zerilli FJ, Armstrong RW. Dislocation-mechanics-based constitutive relations for material dynamics calculations. Journal of Applied Physics 1987;61:1816–25.

[49] Ding Y, Jiang J, Shan A. Plastic instability and strain rate sensitivity of ultrafine-grained iron. Journal of Alloys and Coumpounds 2009;487:517–21.

[50] Tejedor R, Rodriguez-Baracaldo R, Benito JA, Caro J, Cabrera JM. Influence of the carbon content on the strain rate sensitivity of nanocrystalline steels. Scripta Materialia 2008;59:631–4.

[51] Lin MR, Wagoner RH. Effect of temperature, strain, and strain rate on the tensile flow stress of I.F. steel and stainless steel type 310. Scripta Metallurgica 1986;20:143–8.

[52] Thein MA, Lu L, Lai MO. Effects of strain rate on tensile properties of pure Mg and in situ AlN reinforced Mg–5Al composite. Materials Science and Engineering: A 2010;528:239–46.

[53] Lee C Do. Tensile properties of high-pressure die-cast AM60 and AZ91 magnesium alloys on microporosity variation. Journal of Materials Science 2007;42:10032–9.

[54] Yang Q, Ghosh AK. Deformation behavior of ultrafine-grain (UFG) AZ31B Mg alloy at room temperature. Acta Materialia 2006;54:5159–70.

[55] Kim WJ, Lee YG. High-strength Mg – Al – Ca alloy with ultrafine grain size sensitive to strain rate. Materials Science & Engineering A 2011;528:2062–6.

[56] Dallatorre F, Spatig P, Schaublin R, Victoria M. Deformation behaviour and microstructure of nanocrystalline electrodeposited and high pressure torsioned nickel. Acta Materialia 2005;53:2337–49.

[57] Wang Y, Hamza a, Ma E. Temperature-dependent strain rate sensitivity and activation volume of nanocrystalline Ni. Acta Materialia 2006;54:2715–26.

[58] Fan G, Fu L, Choo H, Liaw P, Browning N. Uniaxial tensile plastic deformation and grain growth of bulk nanocrystalline alloys. Acta Materialia 2006;54:4781–92.

[59] Wei Q, Jiao T, Mathaudhu SN, Ma E, Hartwig KT, Ramesh KT. Microstructure and mechanical properties of tantalum after equal channel angular extrusion (ECAE). Materials Science and Engineering: A 2003;358:266–72.

FIGURES

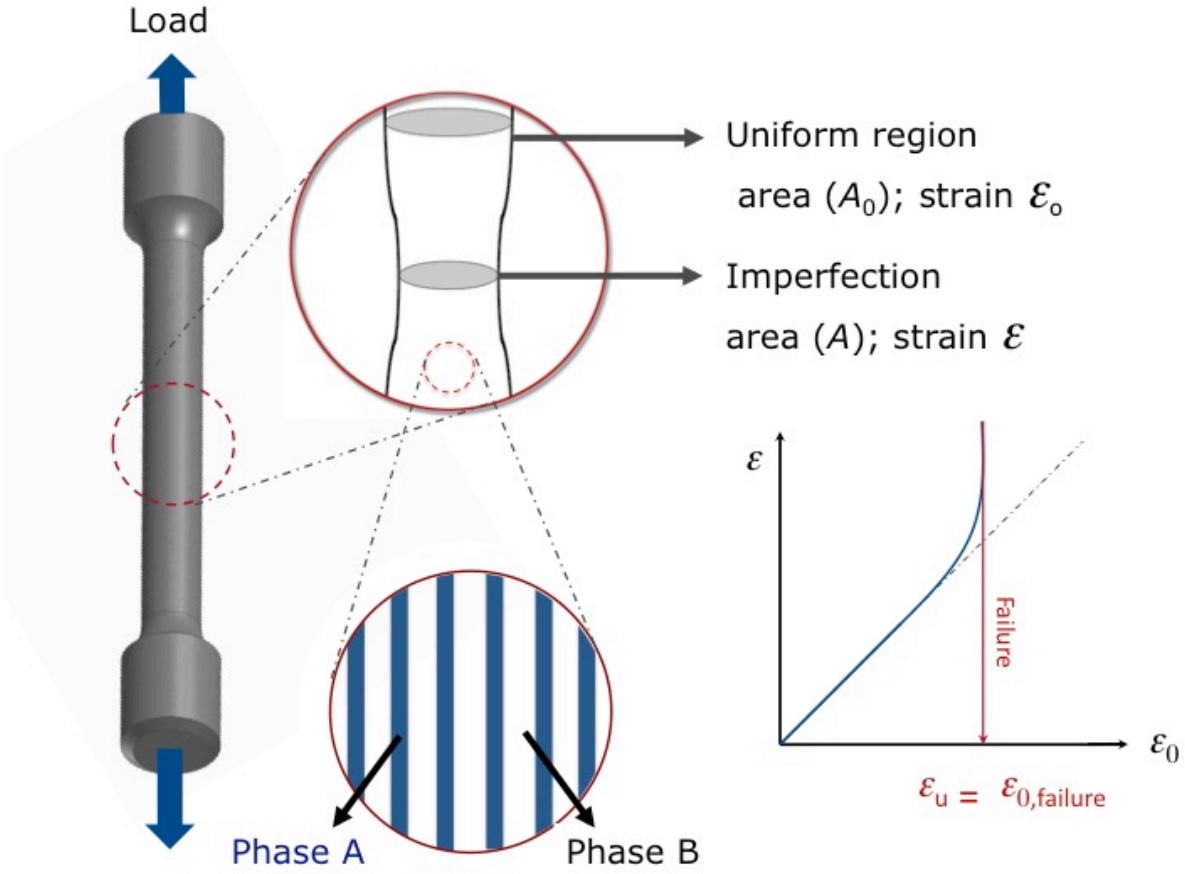

Figure 1: Sketch of a tensile bar of laminated metal composite, and of the geometry assumed in the long wavelength analysis.

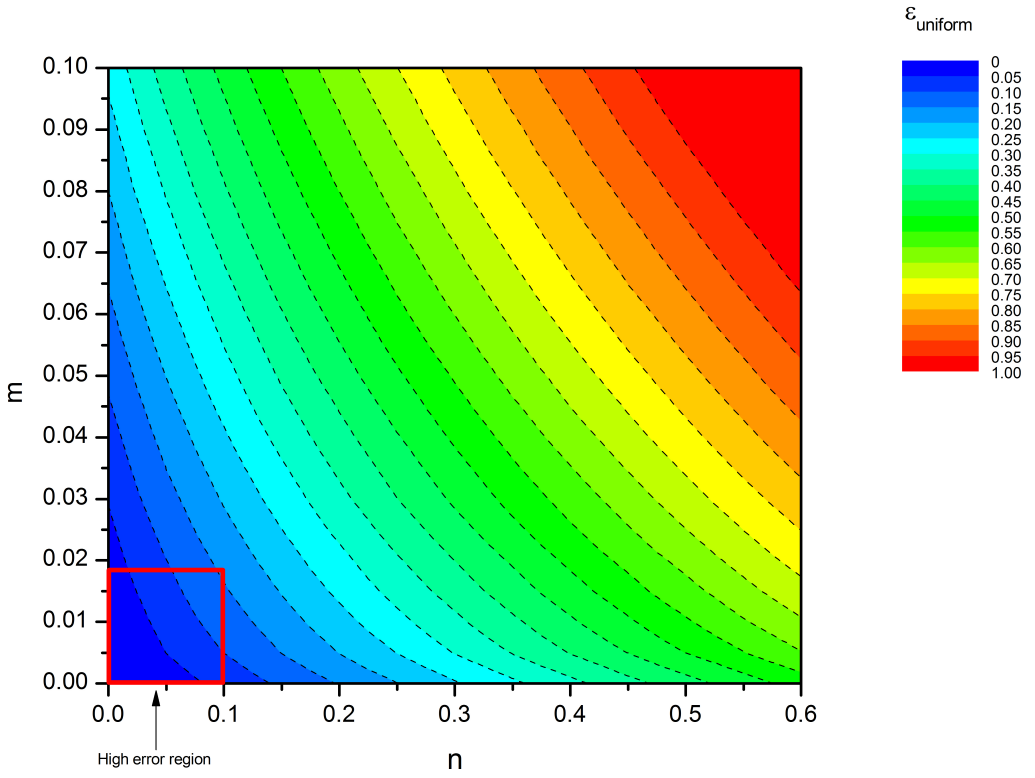

Figure 2: Maximum attainable strain in the uniform section of a power law hardening monolithic material, as a function of its strain hardening exponent n and strain-rate sensitivity m as calculated using the Hutchinson-Neale-Ghosh method for η=0.005 [5].

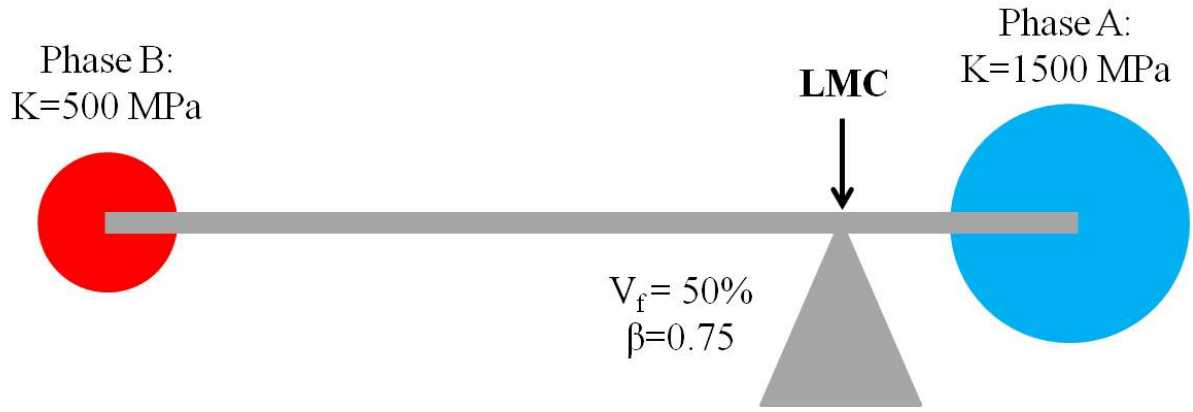

Figure 3: Situating the point corresponding to a composite containing equal phase volume fractions on the (n, m) graph according to the "load-bearing" lever rule dictated by Eqs. (10) and (13).

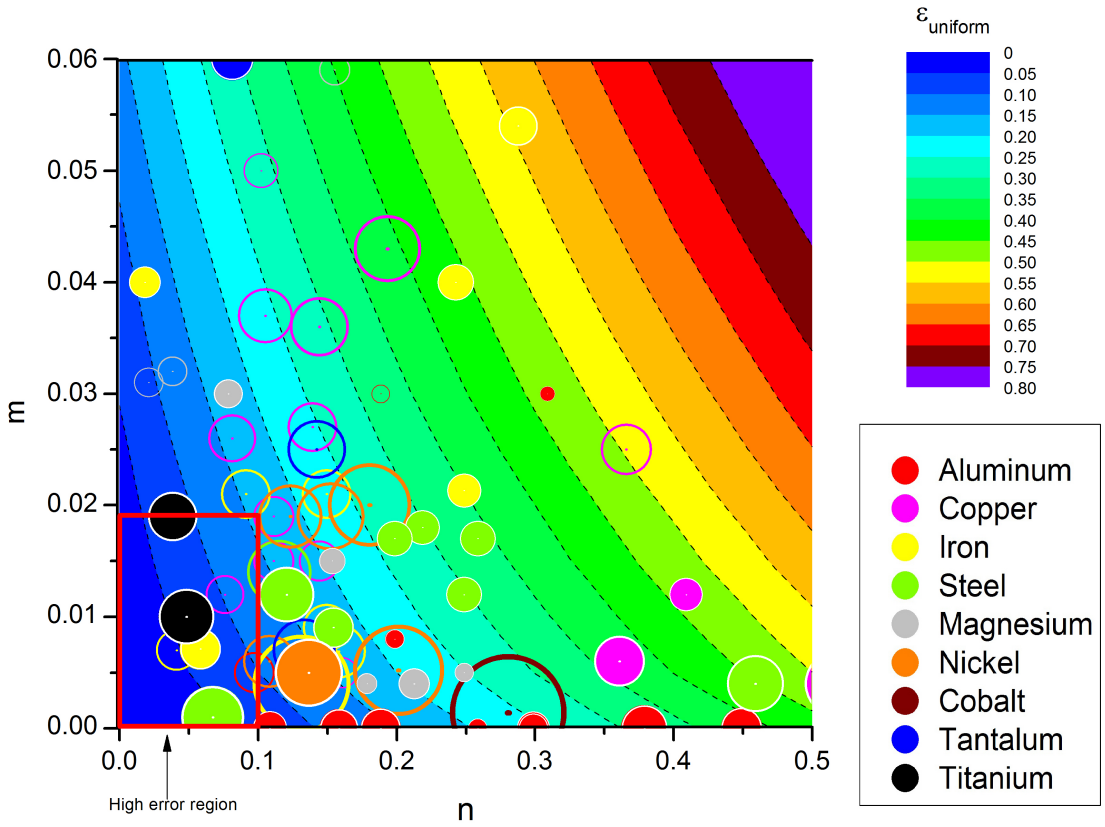

Figure 4: Same graph as in Fig. 2, with superimposed points corresponding to materials listed in Tables 1 to 3. The circle areas are proportional to the strength constant *K*; see Fig. 3 for how to place composite points for equal phase volume fractions. Filled circles represent materials produced by conventional production processes; hollow circles denote more "exotic" alloys (such as nanocrystalline thin films).

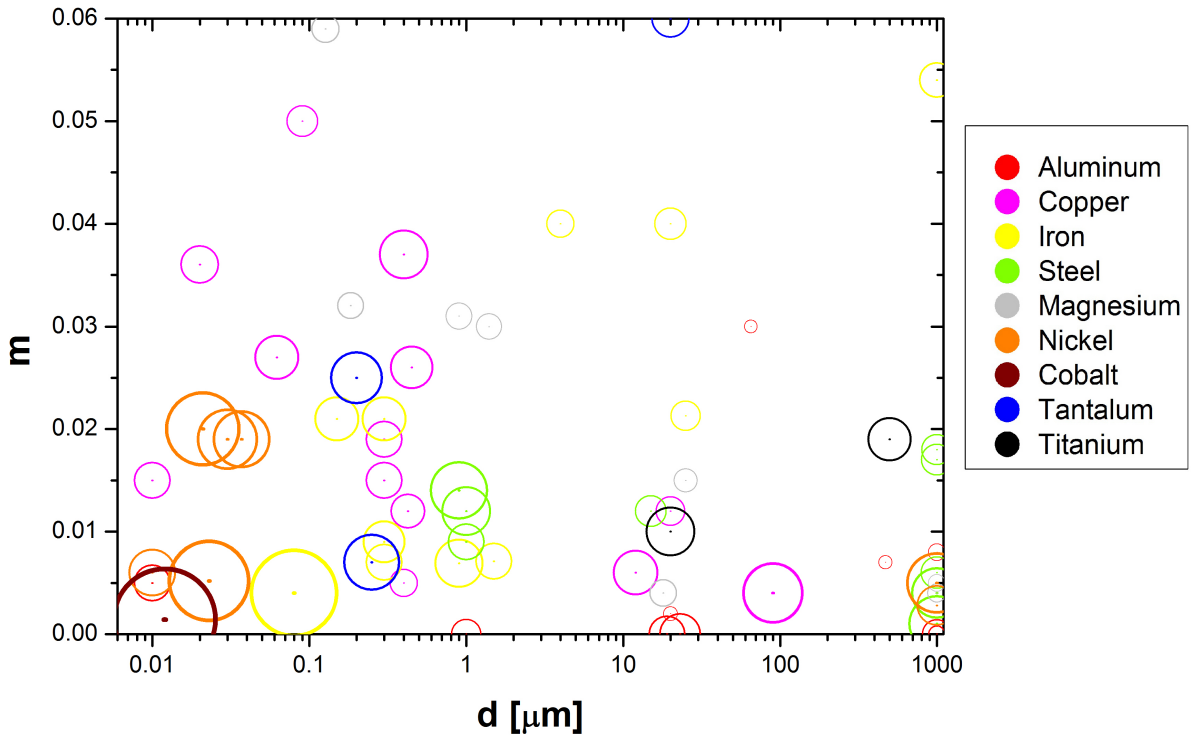

Figure 5: Strain-rate sensitivity *m* for different materials (values given in Tables 1 to 3) as a function of the grain size, *d*. The circle radiuses are proportional to the strength constant *K*. Where references do not give numbers but describe their alloy as coarse-grained, *d* was set to 1000 μm; similarly, where references only describe the metal or alloy as ultra fine grained (UFG) without giving a grain size, *d* was set to 0.01 μm.

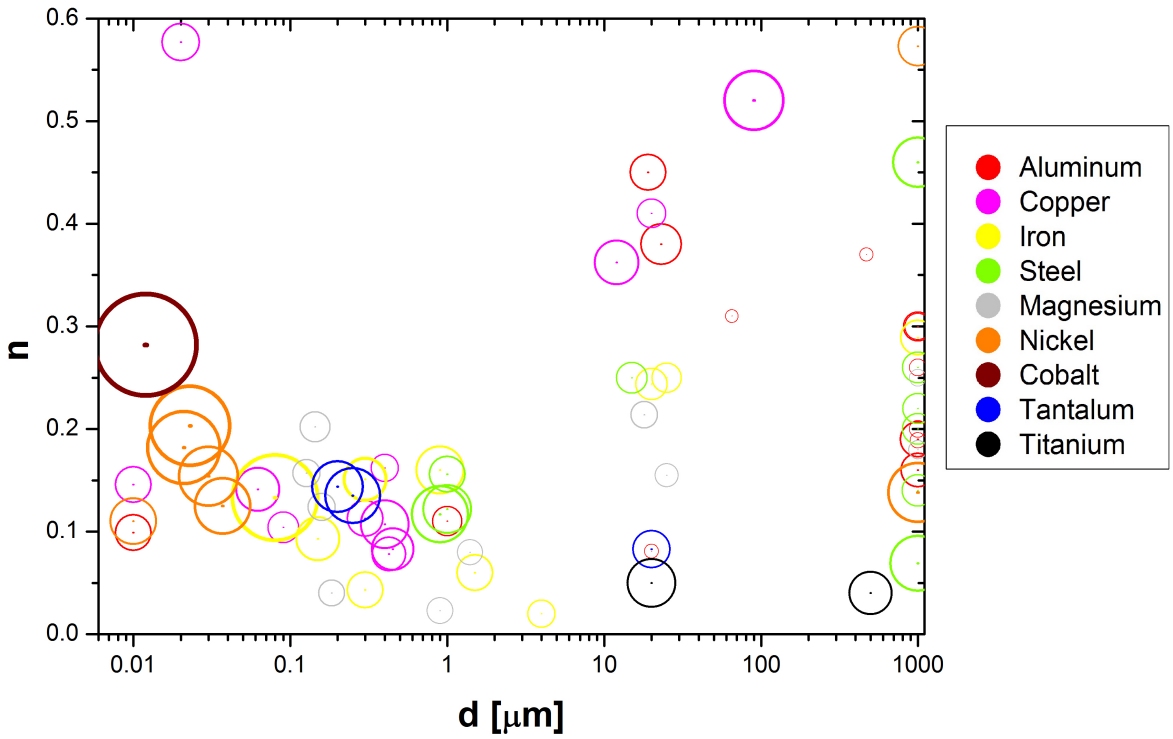

Figure 6: Strain hardening exponent *n* for different materials (values given in Tables 1 to 3) as a function of the grain size, *d*. The circle radiuses are proportional to the strength constant *K*. Where references do not give numbers but describe their alloy as coarse-grained, *d* was set to 1000 μm; similarly, where references only describe the metal or alloy as ultra fine grained (UFG) without giving a grain size, *d* was set to 0.01 μm.

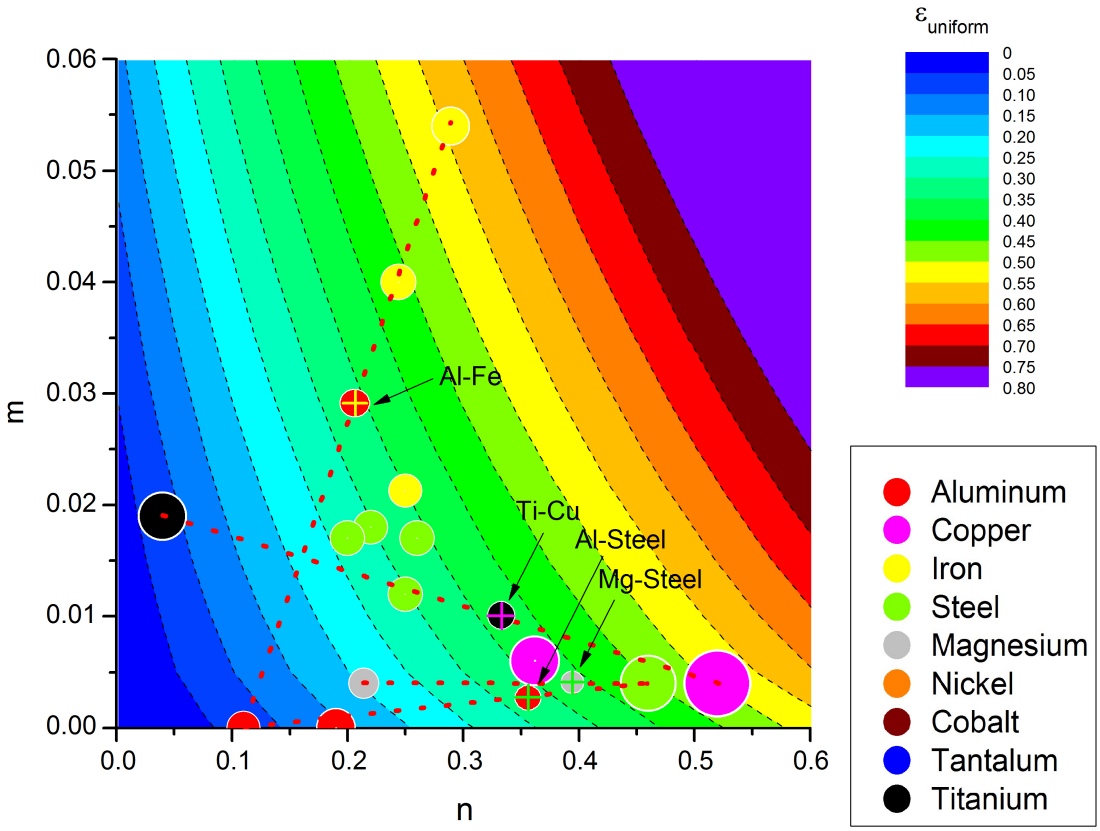

Figure 7: Maximum attainable strain in the uniform section of a power law hardening monolithic materials, as a function of its strain hardening exponent n and strain-rate sensitivity m for η=0.005. Superimposed with the values of practical examples discussed in Section 4. Circle radiuses are proportional to the strength constant K. Composites made of two phases are along the dots lines and corresponds to V_f=0.5. Lines are marked to indicate paired materials, in the same order as the points (*i.e.*, X-Y means that X is to the left, Y to the right of the line).

LIST OF TABLES (THESE APPEAR NEXT PAGE)

Table 1: Physical properties of Aluminum and Copper found in literature. Strain hardening exponent n, strain-rate sensitivity m, strength constant K, for different grain sizes (d), processes and tests strain-rates. Experimental uniform (ε_u EXP) and failure strain ($\varepsilon_{failure}$ EXP) are compared with failure strain calculated by the model used here (ε_u TH).

Table 2: Physical properties of Iron and Steel found in literature. Strain hardening exponent n, strain-rate sensitivity m, strength constant K, for different grain sizes (d), processes and tests strain-rates. Experimental uniform (ε_u EXP) and failure strain ($\varepsilon_{failure}$ EXP) are compared with failure strain calculated by the model used here (ε_u TH).

Table 3: Physical properties of Magnesium, Nickel, Cobalt, Tantalum and Titanium found in literature. Strain hardening exponent n, strain-rate sensitivity m, strength constant K, for different grain sizes (d), processes and tests strain-rates. Experimental uniform (ε_u EXP) and failure strain ($\varepsilon_{failure}$ EXP) are compared with failure strain calculated by the model used here (ε_u TH).

Table 1: Physical properties of Aluminum and Copper found in literature. Strain hardening exponent *n*, strain-rate sensitivity *m*, strength constant *K*, for different grain sizes (*d*), processes and tests strain-rates. Experimental uniform (ε_u EXP) and failure strain ($\varepsilon_{failure}$ EXP) are compared with failure strain calculated by the model used here (ε_u TH).

	Material	n	m	K [MPa]	d [μm]	Strain-rate [s^{-1}]	ε_u EXP	$\varepsilon_{failure}$ EXP	ε_u TH	Process	Ref.
Aluminum	Al 1050	0.081	0.002	130	20	$1.6x10^{-3}$	0.010	0.530	0.067	Annealing	[32]
	Al1100	0.19	0	155	Coarse	-	0.199	0.240	0.144	R+R	[33]
	Al 1100-O	0.20	0.008	180	Coarse	$4.1x10^{-3}$	-	-	0.221	-	[34][35]
	Al 1100-O	0.26	0	179	Coarse	-	-	0.293	0.212	Deep drawing	[36]
	Al 1199	0.31	0.03	108	65	10^{-2}	0.300	0.410	0.469	Wire drawing	[37]
	Al 1199	0.37	0.007	123	470	10^{-2}	0.340	0.410	0.389	Wire drawing	[37]
	Al2008-T4	0.30	0	519	Coarse	$7x10^{-5}$ - $7x10^{-3}$	0.260	-	0.244	Rolled	[38]
	Al 2024-T4	0.16	0	690	Coarse	-	-	-	0.118	-	[34][39]
	Al2024	0.19	0	749	Coarse	-	-	0.157	0.144	Deep drawing	[36]
	Al5052	0.30	0	401	Coarse	-	-	0.207	0.244	Deep drawing	[36]
	Al5052-H32	0.45	0	777	19	$1.3x10^{-3}$	-	-	0.382	-	[12]
	Al6061	0.11	0	548	1	$3x10^{-3}$	0.045	0.057	0.073	Cold rolled	[40]
	Al6061-T6	0.38	0	979	23	$1.3x10^{-3}$	-	-	0.323	-	[12]
	Al 6082	0.19	0	170	Coarse	$1x10^{-4}$	0.190	0.210	0.144	ECAP	[41]
	Al-4Cu-0.5Zr	0.099	0.005	778	UFG	$1x10^{-3}$	-	-	0.099	ECAP	[42]
Copper	Pure Cu	0.113	0.019	766	0.3	-	0.037	-	0.177	ECAP + Rolled	[18]
	Pure Cu	0.113	0.015	766	0.3	-	0.031	-	0.159	Cold rolled	[18]
	Pure Cu	0.146	0.036	1620	0.4-0.5	$6x10^{-4}$	0.052	-	0.292	P. E.	[13]
	Pure Cu	0.367	0.025	1237	0.4-0.5	$6x10^{-4}$	0.017	-	0.506	P. E.	[13]
	Pure Cu	0.152	0.005	449	0.4-0.5	$6x10^{-4}$	0.110	-	0.153	P. E.	[13]
	Pure Cu	0.362	0.006	1184	12	$4x10^{-3}$	0.250	-	0.373	Annealing	[25]
	Pure Cu	0.52	0.004	2168	90	$4x10^{-3}$	0.210	-	0.509	Annealing	[25]
	Pure Cu	0.577	0.036	842	0.02	$6x10^{-4}$	0.520	0.620	0.792	Electro-deposition	[43]
	Pure Cu	0.195	0.043	2092	0.4-0.5	10^{-5}	0.090	0.140	0.389	P. E.	[44]
	Pure Cu	0.107	0.037	1408	0.4	$6x10^{-3}$	0.116	0.140	0.242	P. E.	[45]
	Pure Cu	0.083	0.026	1077	0.45	$6x10^{-3}$	0.056	0.080	0.166	P. E.	[45]
	Pure Cu	0.078	0.012	702	0.425	$6x10^{-3}$	0.022	0.022	0.106	P. E.	[45]
	Pure Cu	0.162	0.005	465	0.4	$6x10^{-3}$	0.152	0.157	0.163	P. E.	[45]
	Pure Cu	0.104	0.05	599	0.09	$1x10^{-5}$	-	0.120	0.288	Powder metallurgy	[46]
	Pure Cu	0.141	0.027	1177	0.062	10^{-6}	0.037	0.120	0.247	Ball milling	[19]
	Pure Cu	0.146	0.015	773	UFG	$1x10^{-3}$	-	-	0.198	ECAP	[42]
	Pure Cu	0.41	0.012	510	20	$7x10^{-4}$	0.250	-	0.469	Cold rolled + Annealed	[47]

R+R: Recrystallization + Rolling
ECAP: Equal Channel Angular Pressing
P. E.: Pulsed Electrodeposition

Table 2: Physical properties of Iron and Steel found in literature. Strain hardening exponent *n*, strain-rate sensitivity *m*, strength constant *K*, for different grain sizes (*d*), processes and tests strain-rates. Experimental uniform (ε_u EXP) and failure strain ($\varepsilon_{failure}$ EXP) are compared with failure strain calculated by the model used here (ε_u TH).

	Material	n	m	K [MPa]	d [μm]	Strain-rate [s^{-1}]	ε_u EXP	$\varepsilon_{failure}$ EXP	ε_u TH	Process	Ref.
Iron	Pure Fe	0.151	0.009	1061	0.3	-	0.058	-	0.174	ECAP	[18]
	Pure Fe	0.043	0.007	788	0.3	-	0.029	-	0.049	ECAP + Rolled	[18]
	Pure Fe	0.133	0.004	4442	0.08	0.015	0.055		0.128	B+C	[15]
	Pure Fe	0.244	0.04	606	20	-	-	-	0.439	B+C	[15]
	Pure Fe	0.151	0.021	1170	0.3	$1x10^{-3}$	0.040	-	0.232	ECAE	[14]
	Pure Fe	0.093	0.021	1148	0.15	$1x10^{-3}$	0.040	-	0.16	ECAE + Rolling	[14]
	Pure Fe	0.289	0.054	730	Coarse	$1x10^{-3}$	-	-	0.56	Annealed	[14][48]
	Pure Fe	0.16	0.0069	1382	0.9	$1x10^{-3}$	0.015	0.058	0.172	A+R+A	[49]
	Pure Fe	0.06	0.0071	786	1.5	$1x10^{-3}$	0.025	0.086	0.067	A+R+A	[49]
	Pure Fe	0.02	0.04	476	4	$1x10^{-3}$	0.040	0.118	0.117	A+R+A	[49]
	Pure Fe	0.25	0.0213	544	25	$1x10^{-3}$	0.210	0.239	0.352	A+R+A	[49]
Steel	Steel sheet	0.25	0.012	585	15	$7x10^{-4}$	0.150	-	0.299	Cold rolled + Annealed	[47]
	Steel - 0.05%C	0.156	0.009	786	1	$1x10^{-4}$	-	-	0.179	Warm Consolidation	[50]
	Steel - 0.3%C	0.122	0.012	1431	1	$1x10^{-4}$	-	-	0.156	Warm Consolidation	[50]
	Steel - 0.55%C	0.117	0.014	1911	0.9	$1x10^{-4}$	-	-	0.16	Warm Consolidation	[50]
	IF Steel	0.22	0.018	566	Coarse	$1x10^{-2}$ - $1x10^{-3}$	-	-	0.3	Cold rolled sheet	[51]
	IF Steel	0.26	0.017	600	Coarse	$7x10^{-5}$ - $7x10^{-3}$	0.280	-	0.34	Rolled	[38]
	SS420J	0.07	0.001	1852	Coarse	$1x10^{-4}$	0.060	0.080	0.051	Annealed	[-]
	SS304	0.46	0.004	1507	Coarse	$1x10^{-4}$	-	0.500	0.451	Annealed	[-]
	UNIVIT Steel (Enameling steel)	0.20	0.017	600	Coarse	$7x10^{-5}$ - $7x10^{-3}$	0.290	-	0.271	Rolled	[38]
	Gainex Steel (Galvanized steel)	0.14	0.006	604	Coarse	$7x10^{-5}$ - $7x10^{-3}$	0.160	-	0.146	Rolled	[38]

ECAP: Equal Channel Angular Pressing
B+C: Bal milling + Consolidated powder
ECAE: Equal Channel Angular Extrusion
A+R+A: Arc melting + Rolled + Annealed

Table 3: Physical properties of Magnesium, Nickel, Cobalt, Tantalum and Titanium found in literature. Strain hardening exponent *n*, strain-rate sensitivity *m*, strength constant *K*, for different grain sizes (*d*), processes and tests strain-rates. Experimental uniform (ε_u EXP) and failure strain ($\varepsilon_{failure}$ EXP) are compared with failure strain calculated by the model used here (ε_u TH).

	Material	n	m	K [MPa]	d [μm]	Strain-rate [s^{-1}]	ε_u EXP	$\varepsilon_{failure}$ EXP	ε_u TH	Process	Ref.
Magnesium	Pure Mg	0.155	0.015	326	25	$3.3x10^{-4}$	0.100	-	0.209	Sintering+ Extrusion	[52]
	Pure Mg	0.04	0.032	421	0.183	$3.3x10^{-4}$	0.080	-	0.124	M+S+E	[52]
	Pure Mg	0.124	0.118	467	0.158	$3.3x10^{-4}$	0.100	-	0.572	M+S+E	[52]
	Pure Mg	0.157	0.059	466	0.127	$3.3x10^{-4}$	0.180	-	0.403	M+S+E	[52]
	Pure Mg	0.202	0.106	559	0.144	$3.3x10^{-4}$	0.330	-	0.653	M+S+E	[52]
	AM60	0.25	0.005	178	Coarse	$2.7x10^{-4}$	0.112	-	0.252	High pressure die casting	[53]
	AZ91	0.18	0.004	215	Coarse	$2.7x10^{-4}$	0.076	-	0.175	High pressure die casting	[53]
	AZ31	0.21	0.004	454	18	$1x10^{-4}$	0.190	0.190	0.205	Rolled + Annealed	[-]
	AZ31B	0.08	0.03	377	1.4	$5.6x10^{-4}$	0.080	0.200	0.176	Hot rolling + ABRC	[54]
	1CaAZ31	0.02	0.031	404	0.9	$1x10^{-4}$	0.030	0.080	0.09	Casting + HRDSR	[55]
Nickel	Pure Ni	0.182	0.02	3250	0.021	$1x10^{-4}$	0.030	-	0.265	Electro-deposition	[56]
	Pure Ni	0.125	0.019	1921	0.037	$1x10^{-4}$	0.017	-	0.191	High pressure tortion	[56]
	Pure Ni	0.573	0.0028	927	Coarse	$1x10^{-4}$	0.400	-	0.547	Cold rolled	[56]
	Pure Ni	0.11	0.006	1318	UFG	$1x10^{-3}$	-	-	0.115	ECAP	[42]
	Pure Ni	0.154	0.019	2155	0.03	$1x10^{-4}$	0.035	0.039	0.227	Electro-deposition	[57]
	Pure Ni	0.138	0.005	2153	Coarse	$1x10^{-4}$	0.040	0.042	0.139	Electro-deposition	[57]
	Ni - 18% Fe	0.203	0.0052	3829	0.023	$1x10^{-3}$	0.050	0.064	0.206	P. E.	[58]
Cobalt	Co-1.65%P	0.282	0.0014	6334	0.012	$1x10^{-3}$	0.014	0.023	0.252	P. E.	[58]
Tantalum	Pure Ta	0.135	0.007	1834	0.25	-	0.040	-	0.146	ECAP +Rolled	[18]
	Pure Ta	0.083	0.06	840	20	$1x10^{-3}$	-	-	0.292	-	[59]
	Pure Ta	0.144	0.025	1591	0.2	$1x10^{-3}$	-	-	0.242	ECAP	[59]
Titanium	Ti-6Al	0.04	0.019	1143	500	$1.7x10^{-5}$-$1.3x10^{-3}$	-	-	0.083	Casting	[24]
	Ti-6Al-2Sn-4Zr-2Mo	0.05	0.01	1430	20	$1.4x10^{-5}$-$1.4x10^{-3}$	-	-	0.066	Forging	[24]

M+S+E: Milling + Sintering + Extrusion
ABRC: Alternate Biaxial Corrugation
HRDSR: High-Ratio Differential Speed Rolling
ECAP: Equal Channel Angular Pressing
P. E.: Pulsed Electrodeposition